

Tensor Network Fluid Simulations in Structured Domains Using the Lattice Boltzmann Method

Lukas Gross,^{1,*} David M. Wawrzyniak,^{2,*} Josef M. Winter,³ Nikolaus A. Adams,^{2,3} and Elie Mounzer¹

¹*German Research Center for Artificial Intelligence,*

Robotics Innovation Center, Robert-Hooke-Str. 1, 28359 Bremen, Germany

²*Technical University of Munich, Munich Institute of Integrated Materials,
Energy and Process Engineering, Lichtenbergstr. 4a, 85748 Garching, Germany*

³*Technical University of Munich, School of Engineering and Design,*

*Chair of Aerodynamics and Fluid Mechanics,
Boltzmannstr. 15, 85748 Garching, Germany*

(Dated: December 9, 2025)

High-fidelity fluid simulations are central to understanding transport phenomena, yet resolving large or geometrically complex systems remains computationally prohibitive with existing methods. Here we introduce a tensor-network formulation of the lattice Boltzmann method based on matrix product states (MPS), commonly known as a quantum-inspired approach, enabling compressed representations of structured flow fields with inherent error control. We demonstrate the generality of the method on flows through structured media and complex vascular geometries, establishing for the first time that tensor-network techniques can efficiently resolve fluid dynamics in complex, irregular domains. We show that in the presence of translational or approximate symmetries of the geometry, fluid states exhibit low effective complexity in MPS form, yielding compression ratios exceeding two orders of magnitude while preserving physical structure and dynamical fidelity. This reduction enables systematic numerical exploration of regimes that were previously intractable. Our results position tensor networks as a scalable paradigm for continuum mechanics.

In computational fluid dynamics (CFD), the Navier-Stokes equations (NSE) are solved to address a variety of engineering and academic problems. To describe complex flow phenomena, a broad range of scales needs to be either resolved directly or appropriately approximated. In direct numerical simulation (DNS), all relevant scales are resolved, which leads to significant computational demand and therefore requires algorithmic compression strategies and the use of high-performance computing systems. Some of the classically used compression strategies for DNS are gradient-based adaptive mesh refinement [1] and wavelet-based multiresolution [2] algorithms [3, 4].

Recently, quantum-inspired compression approaches based on matrix product states (MPS) and the density matrix renormalization group (DMRG) have been introduced as a method for numerical approximation with inherent error control. DMRG [5] and its MPS variants [6–8] are a class of tensor networks, originally developed for efficient simulations of many-body quantum systems with small entanglement [9, 10]. Gourevanov et al. [11] have introduced an algorithm based on MPS decomposition and a DMRG-like approach to variationally solve the incompressible Navier-Stokes equations, drawing an analogy between spatial correlations of quantum states under local Hamiltonians [12] and interscale correlations of turbulent flows. Several extensions have been developed since then. Kiffner and Jaksch [13] introduced resting and moving wall boundary conditions and proposed a more explicit algorithm using a DMRG-like routine [14] to solve the Poisson equation. Peddinti et al. [15] proposed solid boundaries inside the computational domain and efficient evaluation of solutions, while using a similar DMRG-like solver for the Poisson equation. An extension to curvilinear grids was proposed by van Hülst et al. [16], and an implementation for GPUs was proposed by Hölscher et al. [17].

* These authors contributed equally to this work.

Corresponding authors: lukas.gross@dfki.de, elie.mounzer@dfki.de

The lattice Boltzmann method (LBM) is a widely adopted approach for solving the NSE. In this framework, discrete velocity sets are employed to represent single-particle distribution functions. A low Mach-number approximation is achieved through a multiscale expansion, where the collision term can be formulated as a linear relaxation towards an equilibrium using the Bhatnagar–Gross–Krook (BGK) model [18]. This term accounts for local non-equilibrium effects, thereby introducing nonlinearity through an approximated local equilibrium distribution. Compared to directly solving the NSE, LBM exhibits weaker nonlinearity, at the cost of higher dimensionality. In two dimensions, LBM typically evolves nine distinct distribution functions, while in three dimensions it requires at least fifteen, making it a memory-intensive approach. The advection of distribution functions is inherently linear and exact, and implementing complex boundary conditions within the LBM framework is comparatively easy. Moreover, the method inherently employs a uniform computational grid. Although LBM is memory-intensive, few compression techniques have been developed for it [19, 20]. The challenge arises from the coupling between spatial and temporal discretization on uniform grids, which prevents straightforward adaptation of local grid refinement and requires special treatment [21]. These characteristics make LBM an excellent candidate for MPS decomposition. The substantial memory demand associated with storing distribution functions can be effectively mitigated through MPS compression, while preserving the explicit weakly compressible formulation of LBM to circumvent the need to solve a Poisson equation. Furthermore, the uniform grid structure intrinsic to LBM aligns naturally with the MPS representation. Therefore, no additional modifications of the classical LBM algorithm are needed for an MPS-based algorithm.

We propose a novel quantum-inspired method for solving LBM (MPS-LBM) using an MPS-based representation of the distribution functions as MPS, which enables high compression rates while maintaining excellent accuracy. Complex geometries are supported through the incorporation of precomputed boundary masks. Efficient low-rank matrix product operators (MPO) are employed for the streaming step. Additionally, we implement both temporally varying inflow boundary conditions as well as pressure-based outflow conditions. Despite these extensions, MPS-LBM maintains logarithmic scaling in the spatial resolution and quartic scaling in bond dimension characteristic of previous quantum-inspired CFD methods. The proposed algorithm is validated on the example of the Taylor-Green vortex in three dimensions. Furthermore, a three-dimensional simulation of blood flow in a realistic aneurysm geometry, illustrates a typical application of LBM in medical settings. Moreover, an industrially relevant case of flow through pin-fins is presented. Additional test cases are provided in the supplementary material, demonstrating the full capabilities of the proposed algorithm A 1. We find that the pin-fin geometry allows for exceptionally high compression while maintaining high accuracy, highlighting the utility of MPS decompositions in complex flows with industrial relevance.

In summary, we present three key advances:

1. We demonstrate for the first time a quantum-inspired lattice Boltzmann method based on the matrix product state decomposition of the flow variables, including complex inflow boundaries, outflow boundaries, and geometries.
2. We show that the method achieves exceptional compression of translationally symmetric geometries, enabling efficient simulations with excellent accuracy. This demonstrates a major step toward applications of quantum-inspired fluid simulations in industry.
3. Our results underline that fluid simulations based on MPS decompositions perform well in geometries with translational symmetries, which are often encountered in industrial applications such as cooling systems, wind farms, fuel cells, and battery research.

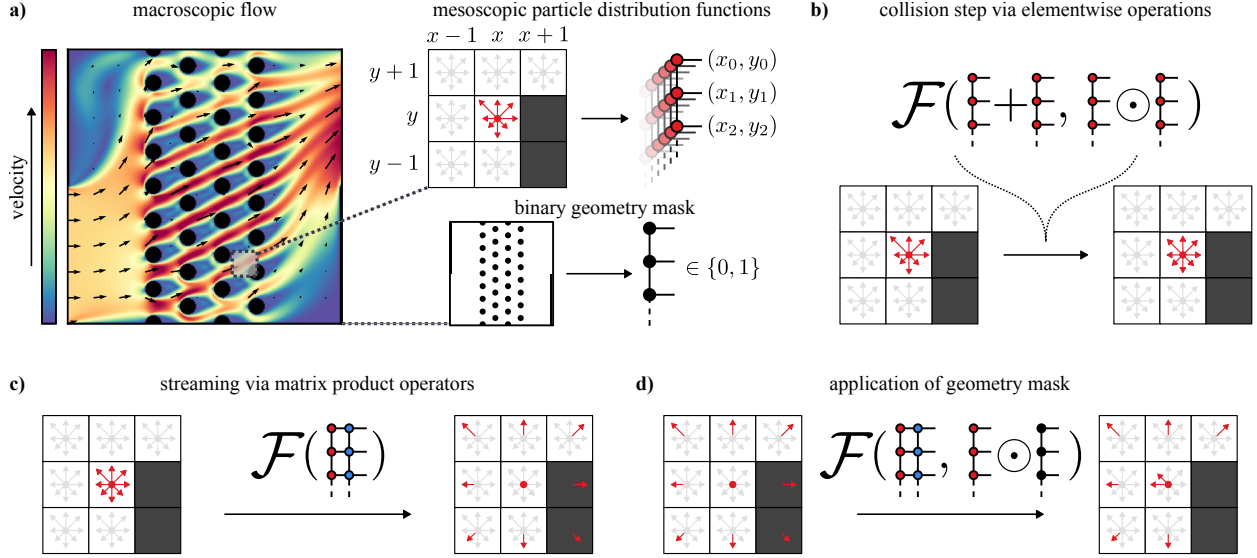


FIG. 1: Overview of the quantum-inspired lattice Boltzmann method. **a)** The macroscopic flow is represented by mesoscopic particle distribution functions (PDF). Each PDF is individually decomposed into a matrix product state (MPS). The geometry is defined by a binary object mask, which is also decomposed into an MPS of the same shape as the PDF. **b)** The collision step models local particle interactions through element-wise operations. These are rewritten in order to be efficiently performed in the MPS-manifold via element-wise summation and multiplication. **c)** The streaming step propagates the PDFs in their respective directions. In the MPS-manifold this step is realized through exact low-rank matrix product operators (MPO). **d)** The interaction with complex geometries is implemented via a bounce-back scheme. MPS-LBM performs this interaction in the MPS-manifold by masking the PDF and applying additional streaming to the masked regions.

I. RESULTS

A. Quantum-Inspired Lattice Boltzmann Method

The lattice Boltzmann method (LBM) provides a mesoscopic approach to fluid dynamics, modeling macroscopic flow governed by the Navier-Stokes equations through discretized *particle distribution functions* (PDF) f_i . Macroscopic quantities such as density ρ and momentum $\rho \mathbf{u}$ are recovered from the hydrodynamic moments [22, 23] of these PDF

$$\rho = \sum_{i=1}^Q f_i(\mathbf{x}, t), \quad \rho \mathbf{u} = \sum_{i=1}^Q \mathbf{c}_i f_i(\mathbf{x}, t), \quad (1)$$

where $Q = |\{\mathbf{c}_i\}|$ denotes the number of discrete microscopic velocities \mathbf{c}_i . The evolution of single components of PDF is governed by the lattice Boltzmann equation [24, 25]

$$f_i(\mathbf{x} + \mathbf{c}_i \Delta t, t + \Delta t) = f_i(\mathbf{x}, t) + \Omega_i(\mathbf{x}, t), \quad (2)$$

with Ω_i representing the collision operator. This process consists of two steps: (i) *collision*, a local relaxation modeling local particle collision by the redistribution of particles among distribution functions f_i (given by the RHS of eq. (2)), and (ii) *streaming*, which propagates PDF along the lattice (shifting of space and time coordinates on the LHS of eq. (2)).

Here, we propose a novel quantum-inspired lattice Boltzmann method (MPS-LBM) based on the MPS framework, leveraging the mostly local formulation of LBM. Distribution functions f_i are spatially discretized on uniform Cartesian meshes. An MPS-decomposition of spatial dimensions, enables compression, reducing the number of variables parameterizing the state with controllable accuracy. Furthermore, local collision interactions can be performed efficiently in the MPS manifold as they consist mostly of element-wise addition [6, 7] and multiplication [26–29], while the streaming step admits an exact formulation as a low-rank matrix product operator (MPO) [30]. See III C for the implementation details and Figure 1 for a schematic overview.

The only exception requiring explicit handling is the calculation of the normalization factor $1/\rho$ when computing the velocity u from the first moment of the PDF in eq. (1). Sanavio and Succi [31] proposed a Taylor expansion of this term around the constant value 1 for a Carleman linearization algorithm of the LBM, for computation on quantum hardware. We build upon this idea by introducing a second-order Taylor expansion of $1/\rho$ around the global mean density ρ_0 at each time step t

$$\frac{1}{\rho} \approx \frac{1}{\rho_0} - \frac{\delta\rho}{\rho_0^2} + \frac{(\delta\rho)^2}{\rho_0^4} + \mathcal{O}((\delta\rho)^3), \quad (3)$$

where $\delta\rho = \rho - \rho_0$ denotes the density fluctuation. The mean density ρ_0 is efficiently computed by contracting the ρ -MPS with a low-rank unit MPS and normalizing the result. For incompressible flows, the relative density fluctuation scales with the Mach number Ma as $\frac{\delta\rho}{\rho_0} \sim \mathcal{O}(\text{Ma}^2)$ in the limit $\text{Ma} \rightarrow 0$ [32]. Consequently, the second-order approximation of $1/\rho$ introduces an error that scales as $\mathcal{O}(\text{Ma}^6)$. The introduced error is several magnitudes lower than the inherent compressibility error $\mathcal{O}(\text{Ma}^2)$ of the LBM [33]. This proposition is further validated by numerical experiments presented in section A 2.

The runtime of our algorithm is dominated by element-wise addition, multiplication, and the application of the low-rank shift MPO. Addition of two MPS is performed by bringing the individual sites of both MPS into a block diagonal structure [6, 8], which yields an MPS of bond dimension 2χ , with χ being the max bond dimension. Reducing the bond dimension via a series of singular value decompositions (SVD) introduces a complexity scaling of $\mathcal{O}(n\chi^3)$ [34] for this operation, where n is the exponent of edge length 2^n on a D -dimensional grid. The application of an MPO to an MPS is done by site-wise contraction of the cores, resulting in an MPS of bond dimension $\chi\chi_{\text{MPO}}$. The MPO for shifting has $\chi_{\text{MPO}} \leq 3$. See A 3 in the supplementary information for an explicit construction of the MPO. Again, a series of SVDs is applied to reduce the bond dimension, resulting in a scaling of $\mathcal{O}(n\chi^3)$. Element-wise multiplication of two MPS is performed using a single-site version of the method from Verstraete et al. [26, 27], with a scaling of $\mathcal{O}(n\chi^4)$. See A 4 for an explicit description. Note that any of the aforementioned primitives can be straightforwardly substituted as advances in fundamental MPS operations become available. In total, we find that our algorithm currently exhibits overall cost scaling of $\mathcal{O}(n\chi^4)$ matching the asymptotic runtime of previous quantum-inspired approaches to CFD. We provide the results of numerical runtime experiments in the supplementary material A 5.

B. Three Dimensional Taylor-Green Vortex

We simulate the three-dimensional Taylor-Green vortex at a Reynolds number of $\text{Re} = 800$ on a grid of size 256^3 . To investigate the impact of compression on simulation accuracy, we conduct experiments using MPS-LBM with different bond dimensions $\chi = \{256, 128, 98, 64\}$. Reference results are obtained using three configurations: (i) a fine LBM on a 256^3 mesh, (ii) fine LBM with a second-order approximation of $1/\rho$ on 256^3 mesh, and (iii) coarse LBM on a 128^3 mesh.

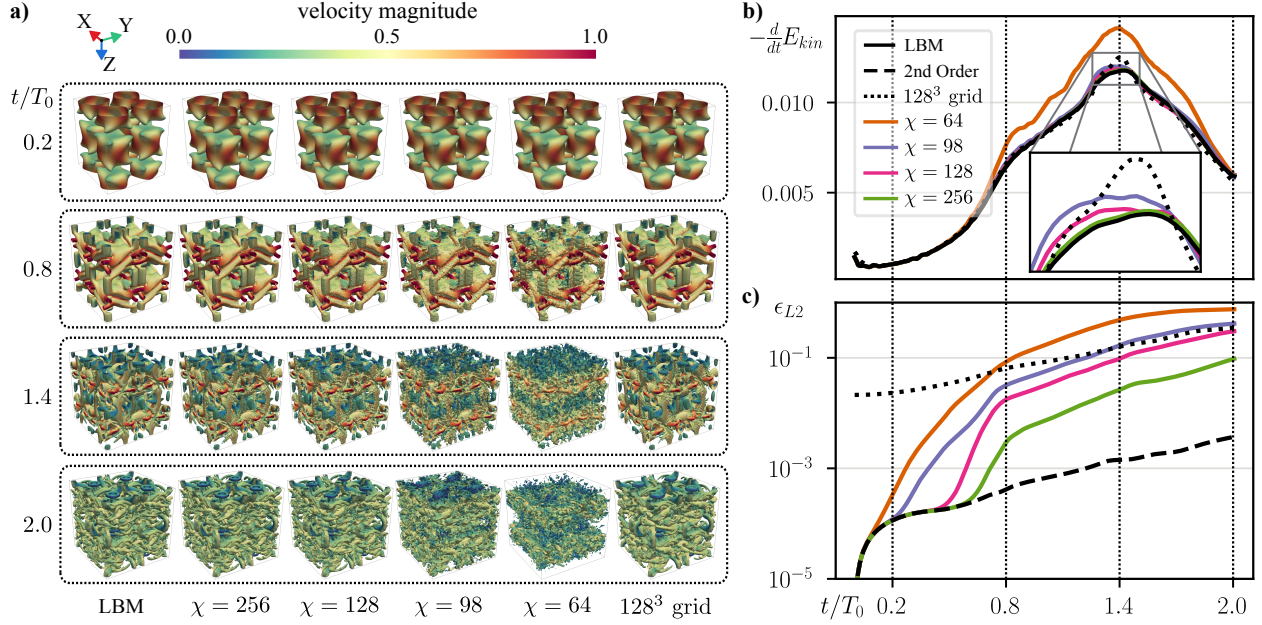


FIG. 2: **Results of the 3D Taylor-Green vortex.** a) Vortical structures, identified by the Q-criterion isosurfaces, are shown at four distinct times $t/T_0 = 0.2, 0.8, 1.4, 2$ for LBM on 256^3 mesh, MPS-LBM with $\chi = 256, 128, 98, 64$, and a coarse LBM. b) Total kinetic energy dissipation $-\frac{d}{dt} E_{kin}$, colored solid lines depict MPS-LBM results, solid black line fine LBM, dotted black line coarse LBM. c) The relative L_2 error ϵ_{L2} with respect to fine LBM. Solid colored lines represent MPS-LBM, dotted black corresponds to coarse LBM. For comparison, the values of fine LBM with second-order approximation of $1/\rho$ are given as the dashed black line.

Figure 2a depicts all simulation results at four different times $t/T_0 = 0.2, 0.8, 1.4, 2.0$, where $T_0 = L/u_0$. Here u_0 denotes the maximum velocity magnitude in the initial conditions, and L is the edge length of the domain. All simulations capture the large-scale structures at time $t/T_0 = 0.2$ well. The solution trajectory deviates from the reference for $\chi = 64$ at $t/T_0 = 0.8$ and for $\chi = 98$ at $t/T_0 = 1.4$, as compression prohibits the formation of smaller-scale structures that emerge later in the flow. Simulations using $\chi = 128$ and $\chi = 256$ reproduce all relevant details throughout the simulation, with $\chi = 128$ showing only minor deviations from fine LBM. In comparison, the coarse LBM falls between the MPS-LBM results with $\chi = 256$ and with $\chi = 128$.

In Figure 2b, the energy dissipation $-\frac{d}{dt} E_{kin}$ is shown. All simulations qualitatively follow the fine LBM and produce physically consistent behavior. The simulation with $\chi = 64$ deviates significantly from the baseline, with the largest errors near the dissipation peak. All MPS-LBM simulations show slightly elevated dissipation before the peak at $t/T_0 \approx 1.3$, while the under-resolved 128^3 LBM exhibits the highest dissipation, marked by a sharp peak at $t/T_0 = 1.4$.

Figure 2c shows the relative error in the L^2 -norm ϵ_{L2} of the macroscopic velocity field for all simulation cases compared to the reference LBM result. As an additional reference, the error of fine LBM with second-order approximation of $1/\rho$ is included. This comparison helps to distinguish the influence of MPS compression from that of the $1/\rho$ approximation. At $t/T_0 = 0.2$, the curve for $\chi = 64$ already separates from the second-order approximation, while higher bond dimensions introduce no noticeable additional inaccuracies. This changes at $t/T_0 = 0.8$, where simulations with lower bond dimensions exhibit higher errors. From that point onward, all simulations show a gradual increase at error, with approximately half an order of magnitude separating $\chi = 64$, $\chi = 98$, and $\chi = 256$. The coarse LBM starts with a substantially higher

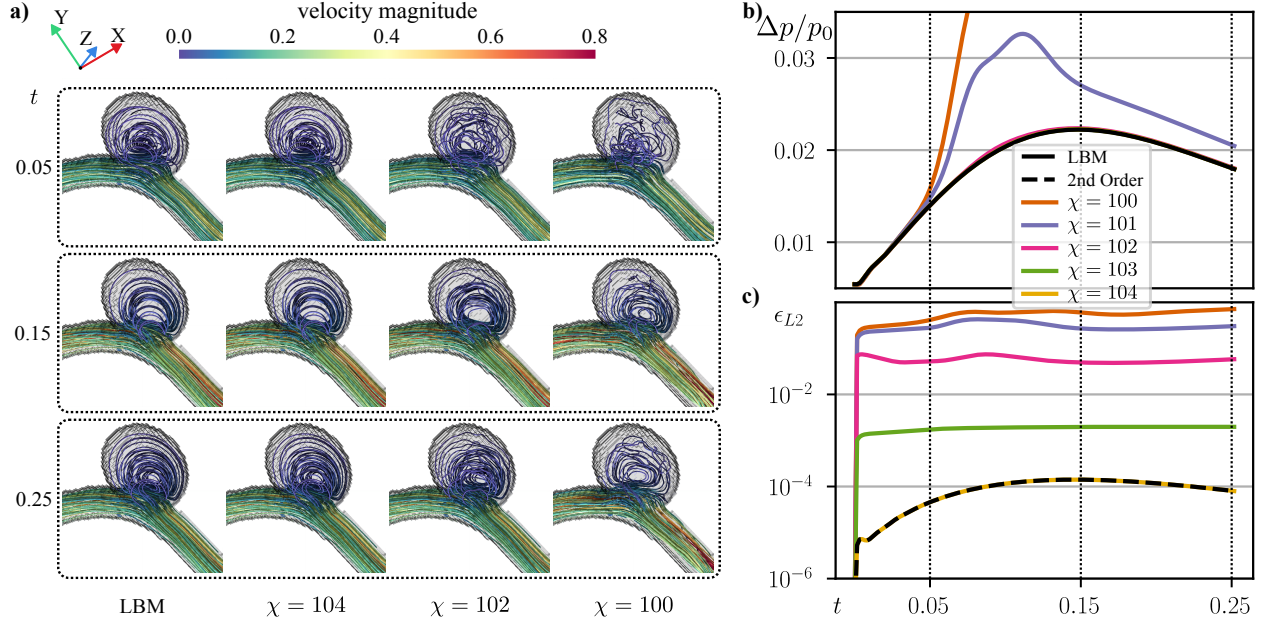


FIG. 3: **Results for flow through a 3D aneurysm.** **a)** Streamlines of the flow at $t = 0.05, 0.15, 0.25$, for the fine LBM (first column) and MPS-LBM at $\chi = 104, 102, 100$ (columns 2-4). **b)** Normalized pressure difference $\Delta p/p_0$ averaged over the region of the aneurysm. **c)** Relative L_2 error ϵ_{L_2} with respect to the fine LBM. Solid colored lines represent MPS-LBM, the solid black line fine LBM, the dashed black line fine LBM with second-order approximation of $1/\rho$.

initial error. However, it matches $\chi = 64$ at $t/T_0 = 0.8$ and $\chi = 98$ at $t/T_0 = 1.4$. The final error at $t/T_0 = 2$ is close to that of MPS-LBM with a bond dimension of $\chi = 128$.

For bond dimensions $\chi = 256$ and $\chi = 128$, the compression ratios are $\text{CR}_{256} \approx 13$ and $\text{CR}_{128} \approx 42$, respectively. A 128^3 grid yields $\text{CR} \approx 8$, while $\chi = 98$ achieves $\text{CR}_{98} \approx 64$, equivalent to a 64^3 grid. Lower grid resolutions are infeasible due to stability issues arising from small relaxation time τ . These results demonstrate that MPS-LBM outperforms simple grid-size reduction in both accuracy and compression efficiency.

C. Aneurysm

To demonstrate the flexibility of MPS-LBM, we simulate blood flow through an aneurysm using time-dependent boundary conditions and a complex geometry encoded via a precomputed MPS boundary mask. Simulations were performed on a 64^3 grid with bond dimensions $\chi = 104, 103, 102, 101, 100$ and compared to uncompressed LBM with exact $1/\rho$ and 2nd-order $1/\rho$ approximated. To isolate the effect of compressing the flow field on the overall accuracy, the mask bond dimension was fixed at $\chi_{\text{mask}} = 98$, which is sufficient to represent the full 64^3 mask to machine precision. The simulation captures the first quarter of a one-second heartbeat, including peak inflow dynamics.

Streamline plots from the LBM simulation at $t = 0.05, 0.15, 0.25$ are shown in the first column of Figure 3a. At $t = 0.05$, the flow exhibits a weak vortical pattern with low velocities. By $t = 0.15$, near peak inflow, the vortex intensifies with higher velocities. At $t = 0.25$, the structure persists but weakens. Compared to this baseline, MPS-LBM at $\chi = 104$ yields nearly identical results. Cases with bond dimensions of $\chi = 100$ and $\chi = 102$ exhibit distorted vortex structures within the aneurysm and fail to reproduce its detailed flow features.

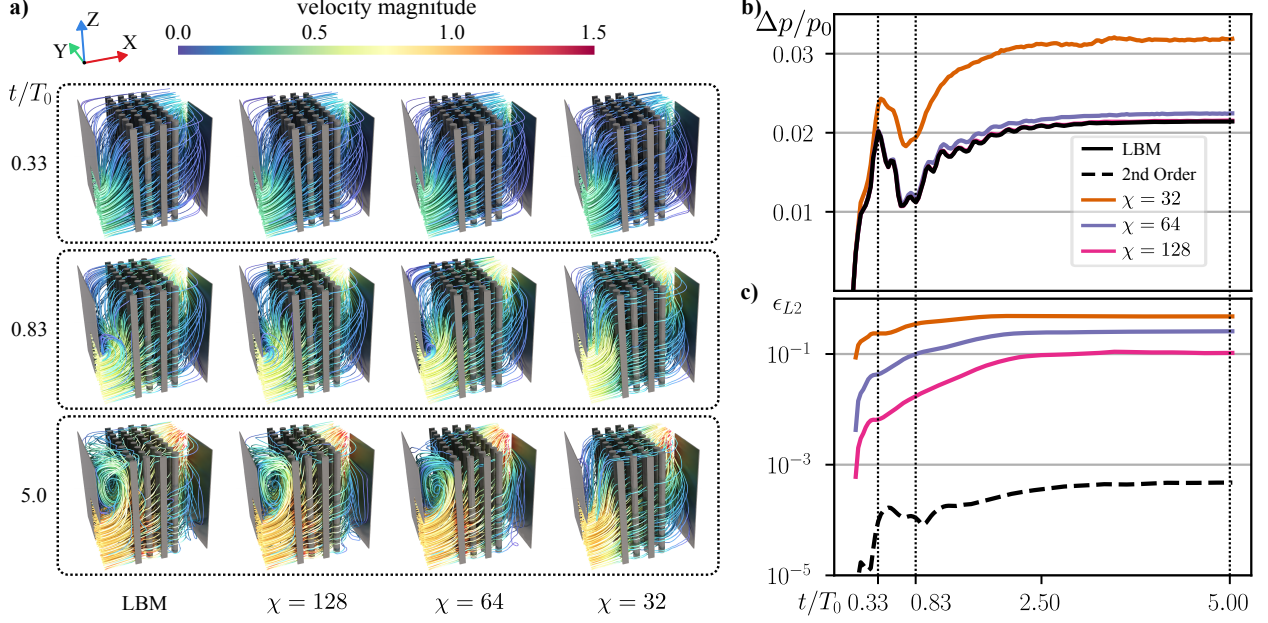


FIG. 4: **Results for flow through pin-fin configuration.** **a)** Streamlines of the flow at $t/T_0 = 0.33, 0.83, 5.0$, for standard LBM (first column) and MPS-LBM at $\chi = 128, 64, 32$ (columns 2-4). **b)** Normalized pressure difference $\Delta p/p_0$ averaged over the inflow region. **c)** Relative L_2 -error ϵ_{L_2} with respect to the standard LBM. Solid colored lines represent MPS-LBM, solid black line standard LBM, the dashed black line standard LBM with second-order approximation of $1/\rho$.

As a relevant measure, we show the average pressure $\Delta p/p_0$ inside the aneurysm normalized with the prescribed outflow pressure in Figure 3b. The standard LBM shows a smooth increase of pressure towards the peak inflow at $t = 0.15$ and a slight decrease afterwards. At $t = 0.05$, the pressures obtained with MPS-LBM at $\chi \leq 101$ diverge from the baseline. At higher bond dimensions, MPS-LBM results are nearly indistinguishable from standard LBM. This suggests that the reproduced vortex structures at $\chi = 102$ can maintain relevant physical aspects of the flow.

The L_2 error ϵ_{L_2} in Figure 3c supports these observations. For $\chi = 100$ and 101 , errors exceed 0.2 and remain high throughout the simulation. At $\chi = 102$, errors drop by nearly an order of magnitude, and at $\chi = 103$ they stabilize around 10^{-3} . With $\chi = 104$, MPS-LBM becomes indistinguishable from LBM with second-order $1/\rho$ approximation, indicating that MPS compression does not introduce significant additional error at this bond dimension.

Notably, the bond dimension χ of the MPS decomposed PDF must exceed χ_{mask} by only a small margin to achieve vanishing errors. However, as χ approaches χ_{mask} , the simulation results quickly deviate strongly from the reference, suggesting that χ_{mask} serves as a lower bound for computationally meaningful χ . At $\chi = 104$, a compression ratio of $\text{CR}_{104} \approx 2.3$ is achieved.

D. Pin-Fin Configuration

A pin-fin array, commonly used in industrial heat exchangers, exhibits translational symmetry and achieves high compression rates with our algorithm. Simulations were conducted on a 256^3 grid. We compare MPS-LBM with bond dimensions $\chi = 128, 64, 32$ to standard LBM with exact and 2nd-order $1/\rho$ approximation. The mask bond dimension was set to $\chi_{\text{mask}} = 16$ to ensure machine-precision accuracy. In-

flow velocity ramps from zero to $u_{\text{in}} = 1$, and simulations run until $t/T_0 = 5$, where $T_0 = L/u_{\text{in}}$, allowing the flow to become steady. The resulting vortex structures reveal that the flow becomes increasingly complex at higher Reynolds numbers.

The streamline plots in Figure 4a depict the velocity field of uncompressed LBM and MPS-LBM simulations. At startup $t/T_0 = 0.33$, all simulations capture the flow accurately. By $t/T_0 = 0.83$, vortices begin to form above the inflow, which are resolved by simulations with $\chi \geq 64$. At the final time $t/T_0 = 5$, all cases except $\chi = 32$ reproduce detailed velocity structures, including the inflow vortex. The $\chi = 32$ simulation fails to capture these features.

The normalized pressure drop $\Delta p/p_0$ from inflow to outflow is shown in Figure 4b. All simulations accurately predict the pressure drop up to $t/T_0 = 0.33$. Beyond this point, $\chi = 32$ overshoots, following the overall trend but overestimating even after convergence to the steady state. Other simulations track the reference closely, with $\chi = 64$ slightly overshooting and $\chi = 128$ matching the pressure drop exactly.

Figure 4c shows a clear separation with respect to the examined bond dimensions in terms of the L_2 -error ϵ_{L_2} of the velocity field. $\chi = 32$ stabilizes around 0.5, $\chi = 64$ around 0.2 and $\chi = 128$ at 0.1. The error of the standard LBM with 2nd-order $1/\rho$ approximation lies below 10^{-3} , clearly showing that in this test case, the errors are dominated by the MPS decomposition.

Putting this in relation to the achieved compression, we find that at $\chi = 64$ with a compression ratio of $\text{CR}_{64} \approx 120$, MPS-LBM maintains an accuracy of 95% in terms of the inflow-outflow pressure difference. At a compression of $\text{CR}_{128} \approx 42$ with $\chi = 128$ the deviation becomes negligible. Although the exact time evolution of the velocity field is not captured by compressed simulations, cases with $\chi \geq 64$ reproduce the pressure difference accurately, indicating that even with high compression rates, the underlying physics is preserved from startup to steady state.

II. DISCUSSION

Quantum-inspired lattice Boltzmann based on matrix product state decomposition (MPS-LBM) addresses the memory bottleneck of LBM while it preserves high accuracy even for complex flow configurations. By compressing the MPS representation, MPS-LBM allows for substantial reductions in memory without altering the main algorithmic structure. The method supports standard inflow/outflow boundary conditions and can handle arbitrary complex three-dimensional geometries within the computational domain, which was not demonstrated with MPS-based approaches before. Its capabilities are demonstrated through three 3D simulations designed to benchmark accuracy, flexibility, and compression performance.

The Taylor–Green vortex benchmark under varying compression ratios demonstrates that already at $\text{CR}_{98} = 64$, the temporal evolution of the kinetic energy is accurately reproduced. With $\text{CR}_{256} = 13$, fully resolved benchmark data are recovered. Complex geometries can be handled, which is shown on the example of the flow in an aneurysm. The compression ratio of the complex geometry mask imposes a lower bound on the achievable compression of the fluid domain, while only a modest increase in bond dimension beyond that of the mask is required to reproduce the flow accurately. A pin-fin array geometry represents the practical application to a heat exchanger. Exploiting translational symmetry, the boundary mask achieves high data compression with accurate predictions. For instance at $\text{CR}_{64} = 120$, pressure drop error is less than 5%, while at $\text{CR}_{128} = 42$ reference data are recovered. Following our discussion in A 6, we anticipate that MPS-LBM delivers high computational performance in settings where the compressibility of translational symmetries can be exploited to reduce computational cost without compromising accuracy, thereby enabling simulations that would otherwise be infeasible due to computational constraints.

Due to the weakly compressible formulation, MPS-LBM does not require iterative solutions of a Poisson equation. Instead, it relies exclusively on element-wise operations within the MPS decomposition,

which ensures that any algorithmic improvements to fundamental MPS operations translate directly into performance gains for MPS-LBM. The modular structure of the underlying LBM framework naturally supports algorithmic extensions, increasing the applicability of MPS-LBM. Heat transport [35], including heat transfer, can be incorporated. Multi-relaxation-time schemes [36] enable higher Reynolds numbers, while multiphase flow models [37] extend the method to chemically relevant systems. Because the MPS decomposition introduces only minimal changes to the core LBM architecture, such extensions are straightforward while significantly expanding the range of MPS-LBM applications.

Another promising direction involves optimizing the decomposition of the binary geometry mask. Instead of minimizing the standard L_2 -norm via singular value decomposition, alternative metrics such as the Hamming distance may be employed. Ideally, the decomposition scheme ensures that the contracted MPS mask remains binary. Advances in this area enable accurate simulations at even higher compression ratios, further extending the efficiency of MPS-LBM.

Finally, the lattice Boltzmann method has recently attracted attention as a candidate for fluid simulations on quantum computers [31, 38, 39]. One of the primary challenges remains the treatment of collision, which is an active area of research [40]. MPS-LBM, particularly the results presented in Section A 2, reduces this nonlinearity to element-wise multiplications with minimal loss of accuracy.

III. METHODS

A. Setup of Numerical Experiments

In LBM, a unit conversion from *physical* to *lattice* units is applied. For all experiments, this conversion is given by the velocity conversion factor $\Delta u = \frac{u_{\text{physical}}}{u_{\text{lattice}}} = \frac{u_0}{\text{Ma } c_s}$. Length is discretized using $\Delta x = \frac{L}{N}$ and the time step is determined by $\Delta t = \frac{\Delta x}{\Delta u}$. Here, u_0 is the characteristic velocity of the flow problem, L is the side length of the domain, and N is the number of lattice sites per side. Two-dimensional and three-dimensional simulations use the D2Q9 and D3Q15 lattice schemes, respectively, which define the lattice speed of sound as $c_s = 1/\sqrt{3}$.

The three-dimensional Taylor-Green vortex is defined on a cube of edge length $L = 2\pi$ and a characteristic velocity $u_0 = 1$ with initial conditions

$$\begin{aligned} u(x, y, z) &= -\sin(x) \cos(y) \cos(z), \\ v(x, y, z) &= \cos(x) \sin(y) \cos(z), \\ w(x, y, z) &= 0, \\ \rho(x, y, z) &= 1 + \frac{1}{16\Delta u^2} (\cos(2x) + \cos(2y)) \cos(2z). \end{aligned} \tag{4}$$

In accordance with similar experiments in [11, 41], we define the Reynolds number using $\text{Re} = \frac{u_0 L}{2\pi\nu}$. All 3D TGV simulations were conducted with $\text{Ma} = 0.1/c_s$ at a resolution of $N^3 = 256^3$.

To ensure realistic flow conditions within the aneurysm geometry, we base our simulation parameters on those reported by Horvat et al. [42], with appropriate adjustments to account for the specifics of our computational setup. The velocities averaged over the inflow surface, ranging between 0.1 m/s and 0.34 m/s, are approximated by $v_{\text{in}}(t) = 0.1 + 18t^{1.5}e^{-10t}$ m/s (see Figure 5a). The domain is a cube of edge length 8 mm discretized at a resolution of $N^3 = 64^3$. The idealized aneurysm geometry is shown in Figure 5b. The aneurysm has a size of approximately $l_{\text{an}} \approx 4\text{mm}$. The relaxation time is given by $\tau = \frac{\text{Ma}N\nu}{Lu_0c_s}$, where $u_0 \approx 0.78$ m/s is the maximum velocity observed at the center of the blood vessel during simulation. The viscosity was adjusted to $\nu = 1.12 \times 10^{-5}$ m²/s to ensure numerical stability of the computational setup.

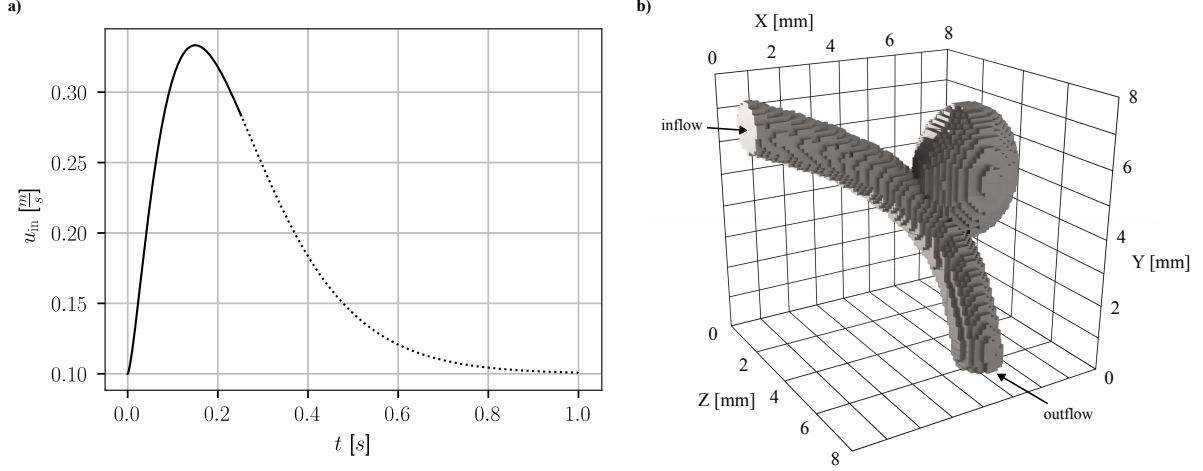


FIG. 5: **Setup of the aneurysm simulation.** **a)** Time-dependent magnitude of the flow velocity at the inflow. The simulations were performed until $t = 0.25$ s depicted by the solid line. For reference, the dotted line shows the remaining part of the 1 s heartbeat cycle. **b)** Full geometry as used in the aneurysm test case. The time-dependent inflow is at $z = 0$, the outflow boundary is at $y = 0$.

This results in a Reynolds number of $Re = \frac{l_{an} u_0}{\nu} \approx 280$. As an initial condition for the PDF, a stationary flow was precomputed using a constant inflow velocity of 0.1 m/s over a duration of 0.15 s.

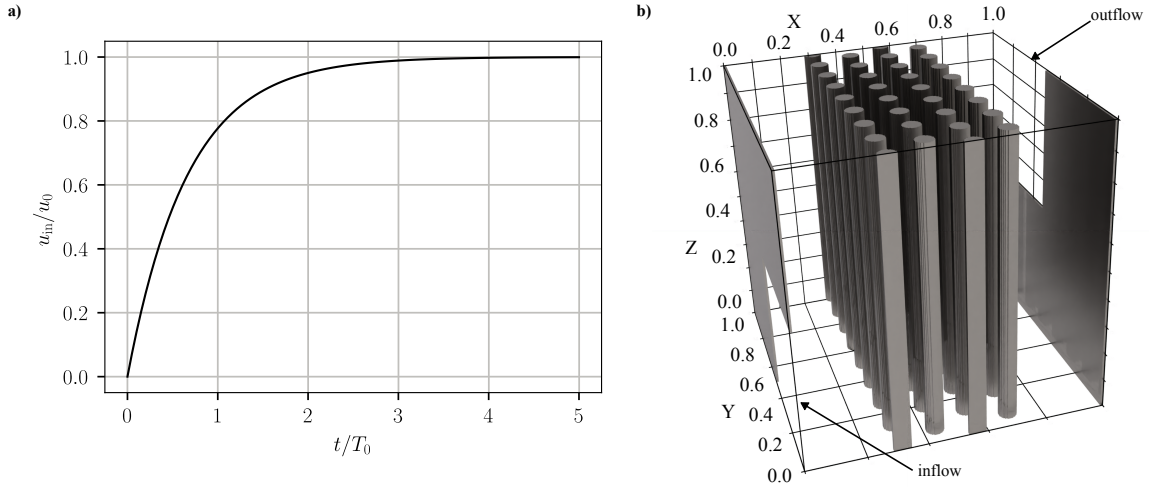


FIG. 6: **Setup of the pin-fin heat sink simulation.** **a)** Time-dependent magnitude of the flow velocity at the inflow. **b)** Full geometry as used in the pin-fin test case. The time-dependent inflow is at $x = 0$, and the outflow boundary is at $x = L$.

In developing the parameterization of the pin-fin heat sink, we follow [43]. To ensure applicability across a range of geometric length scales, the heat-sink configuration is defined on a normalized cubic domain of edge length L (see Figure 6b). The simulation is initiated with a vanishing velocity field, and the inflow velocity is ramped up as $u_{in}(t) = u_0 (1 - \exp(-1.5t))$ (see Figure 6a). The Reynolds number is $Re = \frac{3u_0 L}{16\nu} = 400$ with respect to the distance between the layers of pins $l_{layer} = L/8$ and the maximum velocities occurring towards the end of the simulation of around $u_{max} \approx \frac{3}{2}u_0$. The simulations were run up to $t/T_0 = 5$ with $T_0 = L/u_0$.

B. Metrics for Quantitative Analysis

We evaluate the MPS-LBM accuracy using the relative error of the macroscopic velocity field \mathbf{u} in the L_2 -norm given by

$$\epsilon_{L_2} = \frac{\sqrt{\sum_{d,x} (u_{d,x} - \hat{u}_{d,x})^2}}{\sqrt{\sum_{d,x} \hat{u}_{d,x}^2}}, \quad (5)$$

where $u_{d,x}$ is the result of MPS-LBM, index d is the spatial dimension of the velocity field at position \mathbf{x} and $\hat{u}_{d,x}$ is the reference result.

The total kinetic energy E_{kin} for TGV is given by

$$E_{\text{kin}} = \frac{\rho V_c}{2} \sum_d u_{d,x}^2, \quad (6)$$

where V_c is the volume per lattice site. Density is $\rho = 1/L^3$ such that the total mass is normalized to 1. The total energy dissipation $-\frac{d}{dt} E_{\text{kin}}$ is numerically evaluated using second-order finite differences.

Pressures p are normalized in terms of the prescribed pressure at the outflow p_0 and averaged over the unmasked parts of the region of interest \mathcal{D}

$$\Delta p/p_0 = \frac{1}{p_0 |\mathcal{D}|} \sum_{\mathbf{x} \in \mathcal{D}} (p_{\mathbf{x}} - p_0). \quad (7)$$

In the aneurysm case, we average over the region around the aneurysm $0.53L < x < 0.97L, 0.39L < y < 0.93L, 0.33L < z < 0.69L$. In the pin-fin configuration, we are interested in the pressure drop from inflow to outflow, so we average over the inflow region $0 < x < 2L/256, 0 < y < L/2, 0 < z < L/2$.

The compression ratio CR is

$$\text{CR} = \frac{\text{NVPS}_{\text{ref}}}{\text{NVPS}}, \quad (8)$$

where the number of variables parametrising the solution (NVPS) of a component of the standard LBM on a $(2^n)^D$ grid is $\text{NVPS}_{\text{LBM}} = (2^n)^D$. For MPS-LBM it is given as

$$\text{NVPS}_{\text{QI}} = \sum_{i=1}^n \min\left((2^D)^{i-1}, (2^D)^{n-i+1}, \chi\right) \times 2^D \times \min\left((2^D)^i, (2^D)^{n-i}, \chi\right). \quad (9)$$

C. Details on the Implementation

1. Matrix Product State Representation

All considered scalar fields, i.e., the PDF f_i and macroscopic variables \mathbf{u} and ρ , are discretized on a uniform grid within a computational domain of spatial dimension D . Coordinates are given as integer-valued indices x_d , such that $\sum_d x_d \mathbf{e}_d$ corresponds to the respective continuous coordinate, where \mathbf{e}_d are the basis vectors of the lattice. The number of grid points in each spatial dimension is constrained to 2^n , implying each discretized scalar field to be a tensor $\mathbf{T}^{x_1, \dots, x_D}$ of shape $(2^n)^{\times D}$. Consider the binary representation of the coordinates $x_d = b_d^1 \dots b_d^n$, then \mathbf{T} is represented as an MPS following the scale-ordering procedure introduced in [11] as

$$\mathbf{T}^{x_1, \dots, x_D} = \sum_{\{\alpha\}} (\mathbf{A}_1)_{\alpha_1}^{b_1^1 \dots b_1^D} (\mathbf{A}_2)_{\alpha_1, \alpha_2}^{b_1^2 \dots b_2^D} \dots (\mathbf{A}_n)_{\alpha_{n-1}}^{b_1^n \dots b_D^n}. \quad (10)$$

The tensor (\mathbf{A}_i) is called *core* at *site* i . The maximum extent χ of any index α is called *bond dimension* of the MPS. By SVDs [6–8] χ can be reduced while controlling the induced error, thus compressing the information contained in \mathbf{T}^x .

2. Time Evolution

For simplicity, we employ the BGK collision operator [18] which involves a linear relaxation with rate τ towards an equilibrium f_i^{eq}

$$\Omega_i(\mathbf{x}, t) = \frac{\Delta t}{\tau} (f_i^{eq}(\mathbf{x}, t) - f_i(\mathbf{x}, t)), \quad (11)$$

with the *equilibrium distribution* f^{eq} defined as

$$f_i^{eq}(\mathbf{x}, t) = w_i \rho \left(1 + \frac{\mathbf{u} \cdot \mathbf{c}_i}{c_s^2} + \frac{(\mathbf{u} \cdot \mathbf{c}_i)^2}{2c_s^4} - \frac{\mathbf{u} \cdot \mathbf{u}}{2c_s^2} \right). \quad (12)$$

The *relaxation time* τ is determined by the kinematic viscosity ν via $\tau = \frac{\Delta t}{2} + \frac{\nu}{c_s^2}$. Exploiting the approximation of the inverse density, all operations in the local streaming step are performed in the MPS manifold. Commonly, $\{\mathbf{c}_i\}$ coincides with linear combinations of the basis vectors \mathbf{e}_j of the lattice, such that $\mathbf{c}_i = \sum_d a_{i,d} \mathbf{e}_d$ with $a_{i,d} \in \{-1, 0, 1\}$. Therefore, the streaming step $f_i(\mathbf{x}) \mapsto f_i(\mathbf{x} + \mathbf{c}_i \Delta t)$ can be thought of as the action of a linear operator on the entire tensor

$$f_i^{x_1, \dots, x_D} \mapsto \left(\bigotimes_{d=1}^D \mathbf{S}(a_{i,d}) \right) f_i^{x_1, \dots, x_D}, \quad (13)$$

where \mathbf{S} is the identity for $a_{i,d} = 0$ or an upper (lower) periodic shift matrix for $a_{i,d} = -1$ ($a_{i,d} = 1$). Shift matrices acting on an MPS are efficiently implemented via low-rank MPO for periodic boundary conditions [30]. A detailed derivation is given in A 3.

3. Masking of Objects and Boundaries

In lattice Boltzmann simulations, the computation of immersed objects or non-periodic boundary conditions requires localized computations that only affect cells on the edge of the domain or cells at the boundary of an object. In conventional implementations, these nodes are readily accessible via explicit indexing. However, the inherently non-local and compressed structure of MPS representations prevents direct access to individual boundary cells. Therefore, we employ a strategy based on element-wise addition and multiplication within the MPS manifold. These operations are regulated by binary masks, themselves encoded in MPS form, which specifically select boundary cells, enabling boundary-specific computations.

a. Non-periodic boundaries Non-periodic boundaries are treated by replacing the periodic shift matrices \mathbf{S} used in the streaming step with modified non-periodic shift matrices $\hat{\mathbf{S}}$ at the corresponding boundaries. Conceptually, this introduces zero rows on the set of boundary cells \mathcal{B} corresponding to particle distributions originating outside of the computational domain. Inside the domain, $\hat{\mathbf{S}}$ continues to perform shifts consistent with the streaming operation. We employ a binary mask $m_{\mathcal{B}}^x$, that is 1 for all $x \in \mathcal{B}$ and 0 elsewhere, allowing specific operations on boundary cells. If $x_i = 0$ ($x_i = N$) is a periodic boundary and $a_{i,d} = 1$ ($a_{i,d} = -1$) for some d , then modified streaming

$$f_i^x \mapsto \left(\bigotimes_{d=1}^D \mathbf{S}(a_{i,d}) \right) f_i^x \quad (14)$$

is applied. Otherwise we apply

$$f_i^x \mapsto m_{\mathcal{B}}^x b(f_i^x, \rho_b, \mathbf{u}_b) + \left(\bigotimes_{d=1}^D \hat{\mathbf{S}}(a_{i,d}) \right) f_i^x. \quad (15)$$

Here, $b(f_i^x, \rho_b, \mathbf{u}_b)$ denotes a general boundary function that computes the appropriate values based on the incoming distribution f_i^x , boundary density ρ_b , and velocity \mathbf{u}_b . For a no-slip boundary [44, 45] the function $b_{\text{no-slip}}$ is given by

$$b_{\text{no-slip}}(f_i^x, \rho_b, \mathbf{u}_b) = f_i^x. \quad (16)$$

Dirichlet boundaries with prescribed velocity b_{velocity} are given by

$$b_{\text{velocity}}(f_i^x, \rho_b, \mathbf{u}_b) = f_i^x - \frac{2w_i \rho_b}{c_s^2} \mathbf{c}_i \cdot \mathbf{u}_b, \quad (17)$$

where \mathbf{u}_b is a prescribed macroscopic velocity and ρ_b is the density at the boundary. We approximate $\rho_b = \rho_0$, assuming weak compressibility in the computational domain. Outlet boundaries [46] are computed by describing a wall density ρ_b and using the velocity $\mathbf{u}(x \in \mathcal{B}, t) = \mathbf{u}_b$

$$b_{\text{pressure}}(f_i^x, \rho_b, \mathbf{u}_b) = -f_i^x + 2w_i \rho_b \left(1 + \frac{(\mathbf{c}_i \cdot \mathbf{u}_b)^2}{2c_s^4} - \frac{\mathbf{u}_b \cdot \mathbf{u}_b}{2c_s^2} \right). \quad (18)$$

b. Immersed Objects For immersed objects, we apply the same no-slip condition as defined in Equation 16. However, unlike the approach used for non-periodic boundaries in Equation 15, we do not modify the streaming step directly. Instead, we allow the streaming to proceed as if no obstacle were present, and subsequently reverse the streaming for the solid internal boundary cells. This reversal is conditioned by a binary MPS mask $m_{\mathcal{O}}^x$, which takes the value 1 at all cells $x \in \mathcal{O}$ inside the object and 0 elsewhere.

The implementation is

$$f_i^x \mapsto (1 - m_{\mathcal{O}}^x) f_i^x + \left(\bigotimes_{d=1}^D \mathbf{S}(a_{i,d}) \right) m_{\mathcal{O}}^x f_i^x. \quad (19)$$

While the multiplication with $m_{\mathcal{O}}^x$ ensures only streaming inside the solid object is reversed, $1 - m_{\mathcal{O}}^x$ erases the remaining non-zero entries inside the solid object.

ACKNOWLEDGMENTS

EM and LG would like to thank Hans Hohenfeld, Maximilian Kiefer-Emmanouilidis, and Benedikt Placke for helpful discussions. EM and LG acknowledge funding from the Federal Ministry for Economic Affairs and Energy (BMWE) and the German Aerospace Center (DLR) in the project QuMAL-KI under project number 50RA2208A, and from the Federal Ministry for Research Technology and Space (BMFTR) in the project QuaSA under project number 13N17300 administered by the VDI/VDE Innovation + Technik GmbH (VDI). NAA acknowledges funding from ERC Advanced Grant Project No. 101094463.

AUTHOR CONTRIBUTIONS

The project was conceptualized by DMW, JMW, EM, and NAA, and planned by LG, DMW, JMW, and EM. DMW and LG developed the approximation for inverse density. LG developed, implemented, and

validated the software. Methodological and implementation expertise for LBM was provided by DMW and JMW. Code review and minor development were conducted by DMW. Numerical experiments for the pin-fin heat sink case were planned by DMW and JMW, and those for the aneurysm and TGV cases by LG, DMW, JMW, and EM. LG set up and conducted all numerical experiments and performed data curation. LG and DMW performed post-processing of the data. The results were analyzed and interpreted by LG, DMW, JMW, and EM. DMW and JMW evaluated the physical consistency of the results. LG prepared the figures. The 3D flow visualizations were prepared by JMW and DMW. LG and DMW wrote the manuscript and the supplementary information, with major revisions by DMW. Revisions to the manuscript were conducted by JMW, EM, and NAA. The project was supervised by JMW, EM, and NAA.

DATA AND CODE AVAILABILITY

Associated source code and exemplary data will be published after peer review. The full experimental data will be made available upon reasonable request.

-
- [1] M. Berger and P. Colella, Local adaptive mesh refinement for shock hydrodynamics, [Journal of Computational Physics](#) **82**, 64 (1989).
 - [2] A. Harten, Multiresolution algorithms for the numerical solution of hyperbolic conservation laws, [Communications on Pure and Applied Mathematics](#) **48**, 1305 (1995).
 - [3] N. Hoppe, J. M. Winter, S. Adami, and N. A. Adams, ALPACA - a level-set based sharp-interface multiresolution solver for conservation laws, [Computer Physics Communications](#) **272**, 108246 (2022).
 - [4] L. Han, X. Hu, and N. Adams, Adaptive multi-resolution method for compressible multi-phase flows with sharp interface model and pyramid data structure, [Journal of Computational Physics](#) **262**, 131 (2014).
 - [5] S. R. White, Density matrix formulation for quantum renormalization groups, [Physical Review Letters](#) **69**, 2863 (1992), publisher: American Physical Society.
 - [6] U. Schollwöck, The density-matrix renormalization group in the age of matrix product states, [Annals of Physics January 2011 Special Issue](#), **326**, 96 (2011).
 - [7] I. V. Oseledets, Tensor-Train Decomposition, [SIAM Journal on Scientific Computing](#) **33**, 2295 (2011), publisher: Society for Industrial and Applied Mathematics.
 - [8] R. Orús, A practical introduction to tensor networks: Matrix product states and projected entangled pair states, [Annals of Physics](#) **349**, 117 (2014).
 - [9] G. Vidal, Entanglement Renormalization, [Physical Review Letters](#) **99**, 220405 (2007), publisher: American Physical Society.
 - [10] F. Verstraete, V. Murg, and J. Cirac, Matrix product states, projected entangled pair states, and variational renormalization group methods for quantum spin systems, [Advances in Physics](#) **57**, 143 (2008), <https://doi.org/10.1080/14789940801912366>.
 - [11] N. Gourianov, M. Lubasch, S. Dolgov, Q. Y. van den Berg, H. Babae, P. Givi, M. Kiffner, and D. Jaksch, A quantum-inspired approach to exploit turbulence structures, [Nature Computational Science](#) **2**, 30 (2022), publisher: Nature Publishing Group.
 - [12] J. Eisert, M. Cramer, and M. B. Plenio, Colloquium: Area laws for the entanglement entropy, [Rev. Mod. Phys.](#) **82**, 277 (2010).
 - [13] M. Kiffner and D. Jaksch, Tensor network reduced order models for wall-bounded flows, [Physical Review Fluids](#) **8**, 124101 (2023), publisher: American Physical Society.
 - [14] I. V. Oseledets and S. V. Dolgov, Solution of Linear Systems and Matrix Inversion in the TT-Format, [SIAM Journal on Scientific Computing](#) **34**, A2718 (2012), publisher: Society for Industrial and Applied Mathematics.
 - [15] R. D. Peddinti, S. Pisoni, A. Marini, P. Lott, H. Argentieri, E. Tiunov, and L. Aolita, Quantum-inspired framework for computational fluid dynamics, [Communications Physics](#) **7**, 1 (2024), publisher: Nature Publishing Group.

- [16] N.-L. v. Hülst, P. Siegl, P. Over, S. Bengoechea, T. Hashizume, M. G. Cecile, T. Rung, and D. Jaksch, [Quantum-Inspired Tensor-Network Fractional-Step Method for Incompressible Flow in Curvilinear Coordinates](#) (2025), arXiv:2507.05222 [physics] version: 1.
- [17] L. Hölscher, P. Rao, L. Müller, J. Klepsch, A. Luckow, T. Stollenwerk, and F. K. Wilhelm, Quantum-inspired fluid simulation of two-dimensional turbulence with GPU acceleration, [Physical Review Research](#) **7**, 013112 (2025), publisher: American Physical Society.
- [18] P. L. Bhatnagar, E. P. Gross, and M. Krook, A Model for Collision Processes in Gases. I. Small Amplitude Processes in Charged and Neutral One-Component Systems, [Physical Review](#) **94**, 511 (1954).
- [19] A. Dupuis and B. Chopard, Theory and applications of an alternative lattice Boltzmann grid refinement algorithm, [Physical Review E](#) **67**, 066707 (2003).
- [20] G. Eitel-Amor, M. Meinke, and W. Schröder, A lattice-Boltzmann method with hierarchically refined meshes, [Computers & Fluids](#) **75**, 127 (2013).
- [21] T. Bellotti, L. Gouarin, B. Graille, and M. Massot, Multidimensional fully adaptive lattice Boltzmann methods with error control based on multiresolution analysis, [Journal of Computational Physics](#) **471**, 111670 (2022).
- [22] T. Abe, Derivation of the Lattice Boltzmann Method by Means of the Discrete Ordinate Method for the Boltzmann Equation, [Journal of Computational Physics](#) **131**, 241 (1997).
- [23] X. He and L.-S. Luo, Theory of the lattice Boltzmann method: From the Boltzmann equation to the lattice Boltzmann equation, [Physical Review E](#) **56**, 6811 (1997).
- [24] H. Chen, S. Chen, and W. H. Matthaeus, Recovery of the Navier-Stokes equations using a lattice-gas Boltzmann method, [Physical Review A](#) **45**, R5339 (1992).
- [25] S. Chen and G. D. Doolen, LATTICE BOLTZMANN METHOD FOR FLUID FLOWS, [Annual Review of Fluid Mechanics](#) **30**, 329 (1998).
- [26] F. Verstraete and J. I. Cirac, [Renormalization algorithms for quantum-many body systems in two and higher dimensions](#) (2004), arXiv:cond-mat/0407066 [cond-mat.str-el].
- [27] E. M. Stoudenmire and S. R. White, Minimally entangled typical thermal state algorithms, [New Journal of Physics](#) **12**, 055026 (2010).
- [28] M. Lubasch, P. Moinier, and D. Jaksch, Multigrid Renormalization, [Journal of Computational Physics](#) **372**, 587 (2018), arXiv:1802.07259 [physics].
- [29] A. A. Michailidis, C. Fenton, and M. Kiffner, [Tensor Train Multiplication](#) (2024), arXiv:2410.19747 [physics].
- [30] V. A. Kazeev and B. N. Khoromskij, Low-Rank Explicit QTT Representation of the Laplace Operator and Its Inverse, [SIAM Journal on Matrix Analysis and Applications](#) **33**, 742 (2012).
- [31] C. Sanavio and S. Succi, Lattice boltzmann–carleman quantum algorithm and circuit for fluid flows at moderate reynolds number, [AVS Quantum Science](#) **6**, 023802 (2024).
- [32] X. He and L.-S. Luo, Lattice boltzmann model for the incompressible navier–stokes equation, [Journal of statistical Physics](#) **88**, 927 (1997).
- [33] T. Krüger, H. Kusumaatmaja, A. Kuzmin, O. Shardt, G. Silva, and E. M. Viggien, [The Lattice Boltzmann Method: Principles and Practice](#), Graduate Texts in Physics (Springer International Publishing, Cham, 2017).
- [34] G. Oksa and M. Vajtersic, Multi-level parallelism in the block-jacobi svd algorithm, in [Proceedings Ninth Euro-micro Workshop on Parallel and Distributed Processing](#) (2001) pp. 306–313.
- [35] H. Karani and C. Huber, Lattice boltzmann formulation for conjugate heat transfer in heterogeneous media, [Phys. Rev. E](#) **91**, 023304 (2015).
- [36] D. d’Humières, I. Ginzburg, M. Krafczyk, P. Lallemand, and L.-S. Luo, Multiple-relaxation-time lattice boltzmann models in three dimensions, [Philosophical Transactions of the Royal Society A](#) **360**, 437–451 (2002).
- [37] M. R. Swift, E. Orlandini, W. R. Osborn, and J. M. Yeomans, Lattice boltzmann simulations of liquid-gas and binary fluid systems, [Phys. Rev. E](#) **54**, 5041 (1996).
- [38] A. Tiwari, J. Iaconis, J. Jojo, S. Ray, M. Roetteler, C. Hill, and J. Pathak, [Algorithmic Advances Towards a Realizable Quantum Lattice Boltzmann Method](#) (2025), arXiv:2504.10870 [quant-ph].
- [39] D. Wawrzyniak, J. Winter, S. Schmidt, T. Indinger, C. F. Janßen, U. Schramm, and N. A. Adams, A quantum algorithm for the lattice-Boltzmann method advection-diffusion equation, [Computer Physics Communications](#) **306**, 109373 (2025).
- [40] F. Tennie, S. Laizet, S. Lloyd, and L. Magri, Quantum computing for nonlinear differential equations and turbulence, [Nature Reviews Physics](#) **7**, 220 (2025).

- [41] P. Nathen, D. Gaudlitz, M. Krause, and N. Adams, On the stability and accuracy of the bgk, mrt and rlb boltzmann schemes for the simulation of turbulent flows, [Communications in Computational Physics](#) **23**, 846 (2018).
- [42] M. Horvat, S. B. Lunowa, D. Sytnyk, and B. Wohlmuth, A lattice boltzmann method for non-newtonian blood flow in coiled intracranial aneurysms, in *Numerical Mathematics and Advanced Applications ENUMATH 2023, Volume I*, edited by A. Sequeira, A. Silvestre, S. S. Valtchev, and J. Janela (Springer Nature Switzerland, Cham, 2025) pp. 473–483.
- [43] A. Shahsavar, M. Shahmohammadi, and I. B. Askari, Cfd simulation of the impact of tip clearance on the hydrothermal performance and entropy generation of a water-cooled pin-fin heat sink, [International Communications in Heat and Mass Transfer](#) **126**, 105400 (2021).
- [44] X. He, Q. Zou, L.-S. Luo, and M. Dembo, Analytic solutions of simple flows and analysis of nonslip boundary conditions for the lattice Boltzmann BGK model, [Journal of Statistical Physics](#) **87**, 115 (1997).
- [45] D. P. Ziegler, Boundary conditions for lattice Boltzmann simulations, [Journal of Statistical Physics](#) **71**, 1171 (1993).
- [46] S. Izquierdo and N. Fueyo, Characteristic nonreflecting boundary conditions for open boundaries in lattice Boltzmann methods, [Physical Review E](#) **78**, 046707 (2008).
- [47] X. Shan and H. Chen, Lattice Boltzmann model for simulating flows with multiple phases and components, [Physical Review E](#) **47**, 1815 (1993).
- [48] J. Unfried, J. Hauschild, and F. Pollmann, Fast time evolution of matrix product states using the qr decomposition, [Phys. Rev. B](#) **107**, 155133 (2023).
- [49] J. Bradbury, R. Frostig, P. Hawkins, M. J. Johnson, C. Leary, D. Maclaurin, G. Necula, A. Paszke, J. VanderPlas, S. Wanderman-Milne, and Q. Zhang, [JAX: composable transformations of Python+NumPy programs](#) (2018).
- [50] D. G. a. Smith and J. Gray, opt_einsum - a python package for optimizing contraction order for einsum-like expressions, [Journal of Open Source Software](#) **3**, 753 (2018).

Appendix A: Supplementary Information

1. Two-Dimensional Test Cases

We simulate three benchmark cases: lid-driven cavity, flow around a cylinder, and flow through a porous medium. Each case is computed using both standard LBM and MPS-LBM algorithms at mesh resolutions of 128^2 .

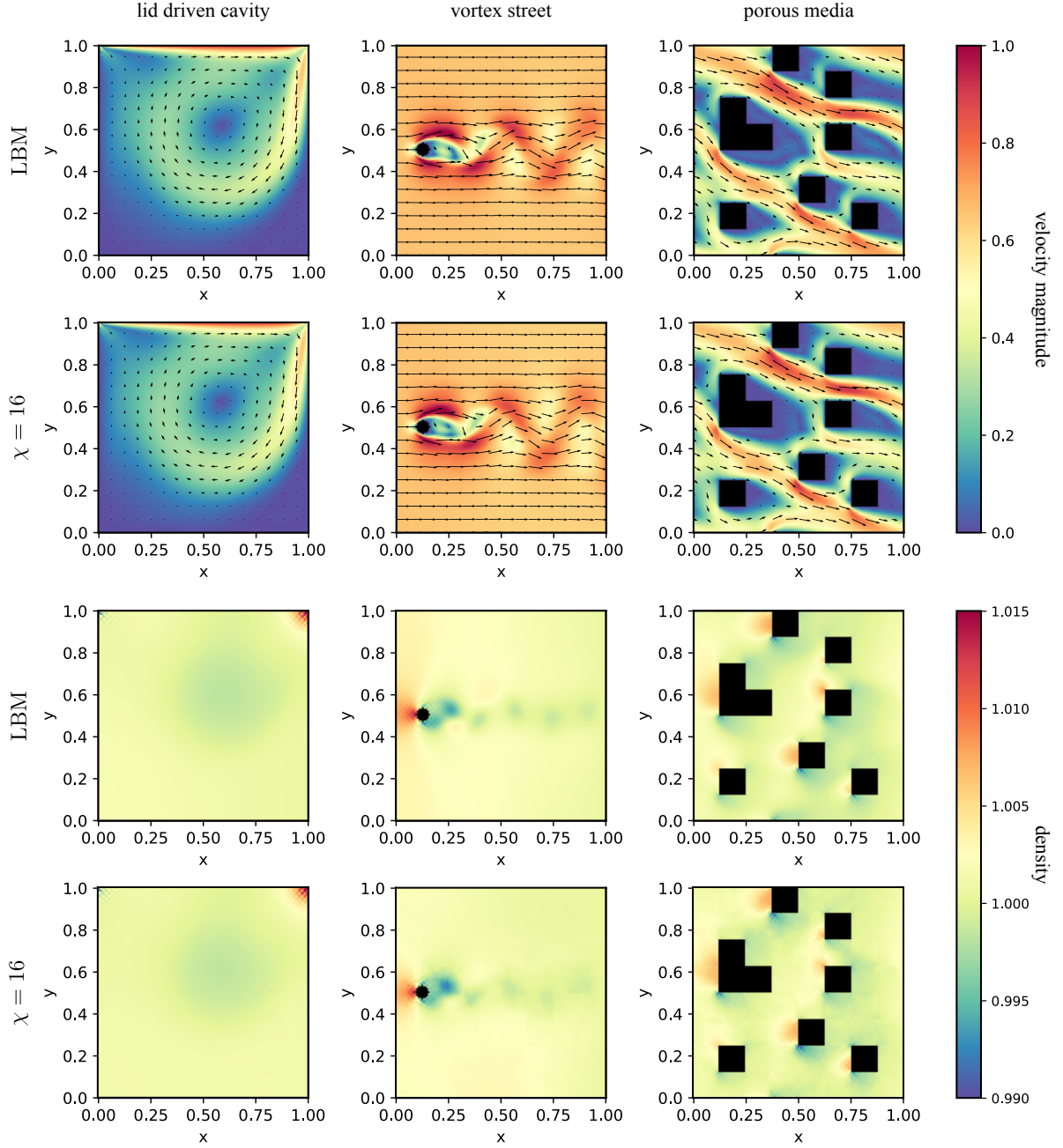


FIG. 7: **Velocity magnitude and density of three common 2D test cases.** Shown from left to right: lid driven cavity, vortex street, and porous media. Top row shows standard LBM simulation, bottom row MPS-LBM at $\chi = 16$ ($CR \approx 4.53$). Color map indicates velocity magnitude / density.

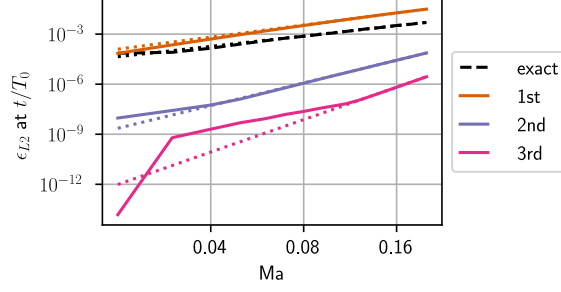


FIG. 8: **Scaling of the L_2 -error ϵ_{L_2} with Mach number Ma .** Results are from simulations of the 2D Taylor-Green vortex at different Ma . Solid colored lines show the error introduced by varying orders of approximation of $1/\rho$ with respect to the standard LBM. The dashed black line depicts the error of standard LBM with respect to the analytic solution of the TGV. Dotted lines indicate the respective linear fit.

All three scenarios are depicted in Figure 7. The bond dimension for all cases is $\chi = 16$, which corresponds to a compression ratio of $CR = 4.53$. The lid-driven cavity is evaluated at time $t = 10 \frac{L}{u_0}$ on a square domain with side length L . The fluid is initially at rest and driven by the top boundary moving at constant velocity, the Reynolds number is $Re = 800$. The flow around a cylinder of diameter d is simulated at Reynolds number $Re = \frac{l_s u_0}{\nu} = 66$. The domain has edge length $L = 16d$, and the velocity magnitude is shown at $t = \frac{5}{3} \frac{L}{u_0}$. Finally, flow through a porous medium is driven by a constant volume force $(F_x, F_y)^T = (0.24, -0.1)^T \text{ N/m}^2$. Following the Shan–Chen forcing scheme [47], forces are incorporated via a perturbation term in the macroscopic velocity, which enters the equilibrium distribution function as

$$\mathbf{u} = \frac{1}{\rho} \sum_i f_i + \frac{\tau \mathbf{F}}{\rho}, \quad (\text{A1})$$

where we apply the same second-order approximation for $1/\rho$. The maximum velocity reaches u_{max} , and the depicted velocity magnitude is shown at $t = 5 \frac{L}{u_{max}}$. For all three scenarios from the reference, a bond dimension of $\chi = 16$ is sufficient to capture the flow dynamics with high fidelity. Only minor deviations are observed in the porous media and cylinder flow case.

2. Approximation of Inverse Density

We conducted a series of two-dimensional Taylor-Green vortex (TGV) simulations with edge length $L = 2\pi$, characteristic velocity $u_0 = 1$, and initial conditions

$$\begin{aligned} u(x, y) &= -\sin(x) \cos(y), \\ v(x, y) &= \cos(x) \sin(y), \\ \rho(x, y) &= 1 + \frac{1}{4\Delta u^2} (\cos(2x) + \cos(2y)). \end{aligned} \quad (\text{A2})$$

The Reynolds number was set to $Re = \frac{u_0 L}{\nu} = 125$. To maintain constant Re while varying Ma , the relaxation time was scaled as $\tau = 0.5 + \frac{N Ma}{c_s Re}$, with $N = 256$ cells per spatial dimension.

The results obtained using Taylor expansions of $1/\rho$ up to third order were compared with standard LBM solutions and the analytical solution of the 2D TGV.

In Figure 8, the colored lines show relative errors of the flow fields in the L_2 -norm ϵ_{L_2} (see subsection III B) of LBM utilizing Taylor expansions of varying order for $1/\rho$ compared to the standard LBM in a log-log plot. The dashed black line indicates ϵ_{L_2} of the exact LBM compared to the analytic solution. Dotted

lines show a linear fit to the respective data in log-log representation. Overall, the second-order approximation offers a favorable trade-off between computational efficiency and numerical accuracy relative to the standard approach.

TABLE I: Fitted exponents of the scaling of ϵ_{L_2} with Mach number.

	Exact	1st	2nd	3rd
Exponent	2.059	2.401	4.513	6.457

The scaling exponents derived from these numerical experiments are summarized in Table I. These were computed via a least squares method. The function $\epsilon_{L_2}(\text{Ma}, \alpha, \beta) = \alpha \text{Ma}^\beta$ was fitted to the computed set of data $(\epsilon_k, \text{Ma}_k)$ by minimizing the sum of squared residuals

$$\min_{\alpha, \beta} \sum_i (\epsilon_k - \epsilon_{L_2}(\text{Ma}_k, \alpha, \beta))^2. \quad (\text{A3})$$

3. Matrix Product Operators for Shifting

The shift MPO applied in the streaming step of the MPS-LBM is based on earlier works [11, 17]. For the sake of completeness, we provide a detailed description of the construction of the shifting MPO, including both cyclic and non-cyclic variants.

Most of this derivation closely follows the considerations of Kazeev et al. [30]. Consider $2^n \times 2^n$ cyclic $\mathbf{S}^{(n)}$ and non-cyclic $\hat{\mathbf{S}}^{(n)}$ shift matrices. As an illustrative example, for $n = 2$, these matrices are defined as

$$\mathbf{S}^{(2)} = \begin{pmatrix} 0 & 1 & 0 & 0 \\ 0 & 0 & 1 & 0 \\ 0 & 0 & 0 & 1 \\ 1 & 0 & 0 & 0 \end{pmatrix}, \quad \hat{\mathbf{S}}^{(2)} = \begin{pmatrix} 0 & 1 & 0 & 0 \\ 0 & 0 & 1 & 0 \\ 0 & 0 & 0 & 1 \\ 0 & 0 & 0 & 0 \end{pmatrix}. \quad (\text{A4})$$

Using the 2×2 matrices

$$I = \begin{pmatrix} 1 & 0 \\ 0 & 1 \end{pmatrix}, \quad J = \begin{pmatrix} 0 & 1 \\ 0 & 0 \end{pmatrix}, \quad J' = \begin{pmatrix} 0 & 0 \\ 1 & 0 \end{pmatrix}, \quad P = \begin{pmatrix} 0 & 1 \\ 1 & 0 \end{pmatrix}, \quad (\text{A5})$$

the shift matrices can be constructed as

$$\begin{aligned} \mathbf{S}^{(2)} &= \begin{pmatrix} J & J' \\ J' & J \end{pmatrix} = I \otimes J + P \otimes J', \\ \hat{\mathbf{S}}^{(2)} &= \begin{pmatrix} J & J' \\ 0 & J \end{pmatrix} = I \otimes J + J \otimes J'. \end{aligned} \quad (\text{A6})$$

The corresponding $2^3 \times 2^3$ matrices can be expressed in terms of $\mathbf{S}^{(2)}$ and $\hat{\mathbf{S}}^{(2)}$ as

$$\begin{aligned} \mathbf{S}^{(3)} &= \begin{pmatrix} \hat{\mathbf{S}}^{(2)} & J'^{\otimes 2} \\ J'^{\otimes 2} & \hat{\mathbf{S}}^{(2)} \end{pmatrix} = I \otimes \hat{\mathbf{S}}^{(2)} + P \otimes J'^{\otimes 2}, \\ \hat{\mathbf{S}}^{(3)} &= \begin{pmatrix} \hat{\mathbf{S}}^{(2)} & J'^{\otimes 2} \\ 0 & \hat{\mathbf{S}}^{(2)} \end{pmatrix} = I \otimes \hat{\mathbf{S}}^{(2)} + J \otimes J'^{\otimes 2}, \end{aligned} \quad (\text{A7})$$

leading to the recursive definition

$$\begin{aligned} \mathbf{S}^{(n)} &= \begin{pmatrix} \hat{\mathbf{S}}^{(n-1)} & J'^{\otimes(n-1)} \\ J'^{\otimes(n-1)} & \hat{\mathbf{S}}^{(n-1)} \end{pmatrix} = I \otimes \hat{\mathbf{S}}^{(n-1)} + P \otimes J'^{\otimes(n-1)}, \\ \hat{\mathbf{S}}^{(n)} &= \begin{pmatrix} \hat{\mathbf{S}}^{(n-1)} & J'^{\otimes(n-1)} \\ 0 & \hat{\mathbf{S}}^{(n-1)} \end{pmatrix} = I \otimes \hat{\mathbf{S}}^{(n-1)} + J \otimes J'^{\otimes(n-1)}. \end{aligned} \quad (\text{A8})$$

We introduce the rank core product as defined in [30]. Consider 4-dimensional tensors $\mathbf{A}_{\alpha\beta}^{ab}$ and $\mathbf{B}_{\alpha\beta}^{ab}$, and explicitly expand the upper indices as

$$\begin{bmatrix} \mathbf{A}_{11} & \mathbf{A}_{12} & \dots \\ \mathbf{A}_{21} & \mathbf{A}_{22} & \dots \\ \vdots & \vdots & \ddots \end{bmatrix}, \quad \begin{bmatrix} \mathbf{B}_{11} & \mathbf{B}_{12} & \dots \\ \mathbf{B}_{21} & \mathbf{B}_{22} & \dots \\ \vdots & \vdots & \ddots \end{bmatrix}, \quad (\text{A9})$$

where each entry is a 2-dimensional tensor. The rank core product “ \bowtie ” of these two tensors is

$$\begin{bmatrix} \mathbf{A}_{11} & \mathbf{A}_{12} \\ \mathbf{A}_{21} & \mathbf{A}_{22} \end{bmatrix} \bowtie \begin{bmatrix} \mathbf{B}_{11} & \mathbf{B}_{12} \\ \mathbf{B}_{21} & \mathbf{B}_{22} \end{bmatrix} = \begin{bmatrix} \mathbf{A}_{11} \otimes \mathbf{B}_{11} + \mathbf{A}_{12} \otimes \mathbf{B}_{21} & \mathbf{A}_{11} \otimes \mathbf{B}_{12} + \mathbf{A}_{12} \otimes \mathbf{B}_{22} \\ \mathbf{A}_{21} \otimes \mathbf{B}_{11} + \mathbf{A}_{22} \otimes \mathbf{B}_{21} & \mathbf{A}_{21} \otimes \mathbf{B}_{12} + \mathbf{A}_{22} \otimes \mathbf{B}_{22} \end{bmatrix}. \quad (\text{A10})$$

For connecting this to MPO. Consider a 3-dimensional Tensor $\mathbf{T} \in \mathbb{R}^3$ and a linear operator

$$\begin{aligned} \mathbf{O} : \mathbb{R}^3 &\rightarrow \mathbb{R}^3 \\ \mathbf{T}^{abc} &\mapsto \sum_{a,b,c} \mathbf{O}^{def,abc} \mathbf{T}^{abc}. \end{aligned} \quad (\text{A11})$$

In accordance to eq. (10), we define the MPO decomposition of \mathbf{O} as

$$\mathbf{O}^{abc,def} = \sum_{\alpha,\beta} \mathbf{A}_{\alpha}^{ad} \mathbf{B}_{\alpha\beta}^{be} \mathbf{C}_{\beta}^{cf}, \quad (\text{A12})$$

which can be written in terms of the core rank product as

$$\mathbf{O} = \mathbf{A} \bowtie \mathbf{B} \bowtie \mathbf{C}. \quad (\text{A13})$$

Similarly we decompose \mathbf{S} and $\hat{\mathbf{S}}$ with the rank core product and rewrite eq. (A8) as

$$\begin{aligned} \mathbf{S}^{(n)} &= \begin{bmatrix} I & P \end{bmatrix} \bowtie \begin{bmatrix} \hat{\mathbf{S}}^{(n-1)} \\ J'^{\otimes(n-1)} \end{bmatrix}, \\ \hat{\mathbf{S}}^{(n)} &= \begin{bmatrix} I & J \end{bmatrix} \bowtie \begin{bmatrix} \hat{\mathbf{S}}^{(n-1)} \\ J'^{\otimes(n-1)} \end{bmatrix}, \end{aligned} \quad (\text{A14})$$

which already signifies that only the first core different for cyclic and non-cyclic shift MPO. $\hat{\mathbf{S}}$ can be further decomposed as

$$\begin{aligned} \hat{\mathbf{S}}^{(n)} &= \begin{bmatrix} I & J \end{bmatrix} \bowtie \begin{bmatrix} I & J \\ 0 & J' \end{bmatrix} \bowtie \begin{bmatrix} \hat{\mathbf{S}}^{(n-2)} \\ J'^{\otimes(n-2)} \end{bmatrix} \\ &= \begin{bmatrix} I & J \end{bmatrix} \bowtie \underbrace{\begin{bmatrix} I & J \\ 0 & J' \end{bmatrix} \bowtie \dots \bowtie \begin{bmatrix} I & J \\ 0 & J' \end{bmatrix}}_{(n-2)\text{-times}} \bowtie \begin{bmatrix} \hat{\mathbf{S}}^{(1)} \\ J' \end{bmatrix}. \end{aligned} \quad (\text{A15})$$

Using $\hat{\mathbf{S}}^{(1)} = J$ we can define

$$\mathbf{A} = \begin{bmatrix} I & P \end{bmatrix}, \quad \hat{\mathbf{A}} = \begin{bmatrix} I & J \end{bmatrix}, \quad \mathbf{B} = \begin{bmatrix} I & J \\ 0 & J' \end{bmatrix}, \quad \mathbf{C} = \begin{bmatrix} J \\ J' \end{bmatrix}, \quad (\text{A16})$$

such that

$$\begin{aligned} \mathbf{S}^{(n)} &= \mathbf{A} \bowtie \mathbf{B} \bowtie \cdots \bowtie \mathbf{B} \bowtie \mathbf{C}, \\ \hat{\mathbf{S}}^{(n)} &= \hat{\mathbf{A}} \bowtie \mathbf{B} \bowtie \cdots \bowtie \mathbf{B} \bowtie \mathbf{C}. \end{aligned} \quad (\text{A17})$$

It is straightforward to show that a shift in the opposite direction is achieved by simply interchanging J with J' and vice versa in all cores.

The above derivation only produces shift matrices on vectors; however, for MPS-LBM, we need to shift in all dimensions of the flow tensor separately. Note that in eq. (10), the indices are split into binary digits such that the i -th bit of each core corresponds to the i -th dimension. Thus, the cores of the shift MPO are to act on the i -th index only to result in a shift in the i -th dimension. This is achieved by padding the individual cores with identities. Say we want a shift in the first of three dimensions, then the first core of the respective MPO is

$$A \bowtie \begin{bmatrix} I & 0 \\ 0 & I \end{bmatrix} \bowtie \begin{bmatrix} I & 0 \\ 0 & I \end{bmatrix}, \quad (\text{A18})$$

and analogously \mathbf{B} and \mathbf{C} are padded.

4. Elementwise Multiplication

In this subsection, we explicitly describe the algorithm used for element-wise multiplication with included compression. We also briefly discuss possible alternatives. In this work, we employed the single-site version of the algorithm proposed in [26]. Consider the element-wise product of two MPS \mathbf{B} and \mathbf{C} and a candidate MPS \mathbf{A} , that has the desired bond dimension. The idea is to fit \mathbf{A} to $\mathbf{B} \odot \mathbf{C}$ by minimizing the squared L_2 -norm

$$\begin{aligned} &\min_{\mathbf{A}} \|\mathbf{A} - (\mathbf{B} \odot \mathbf{C})\|_2^2, \\ &\Leftrightarrow \nabla_{\mathbf{A}} \|\mathbf{A} - (\mathbf{B} \odot \mathbf{C})\|_2^2 = 0, \\ &\Leftrightarrow \nabla_{\mathbf{A}} (\mathbf{A} \cdot \mathbf{A}) - \nabla_{\mathbf{A}} (2\mathbf{A} \cdot (\mathbf{B} \odot \mathbf{C})) + \underbrace{\nabla_{\mathbf{A}} ((\mathbf{B} \odot \mathbf{C}) \cdot (\mathbf{B} \odot \mathbf{C}))}_{=0} = 0. \end{aligned} \quad (\text{A19})$$

With Kronecker delta tensors $\delta^{i,j,k}$, we can write the element-wise product as the tensor network diagram shown in Figure 9a (for an introduction to the diagrammatic language of tensor networks, we refer to [8]). Now let \mathbf{A} be in canonical form with the center at site c , that is

$$\mathbf{A}^{x_1, \dots, x_c, \dots, x_D} = \sum_{\{\alpha\}} (\mathbf{U}_1)_{\alpha_1}^{x_1} \cdots (\mathbf{A}_c)_{\alpha_{c-1}, \alpha_c}^{x_c} \cdots (\mathbf{V}_n)_{\alpha_{n-1}}^{x_n}, \quad (\text{A20})$$

where $\mathbf{U}\mathbf{U}^\dagger = \mathbf{V}\mathbf{V}^\dagger = \mathbb{I}$. Then $\mathbf{A} \cdot \mathbf{A}$ reduces to the scalar product of \mathbf{A}_c with itself as in Figure 9b. Instead of the gradient with respect to the whole of \mathbf{A} in eq. (A19), we consider the local gradient at site c , and derive the respective tensor network as in Figure 9c. The local minimum is found by setting \mathbf{A}_c equal to the contraction of the right-most term in Figure 9c. Minimization is achieved iteratively as in Figure 9d: Contract the tensor network, replace the canonical center, shift the canonical center, and

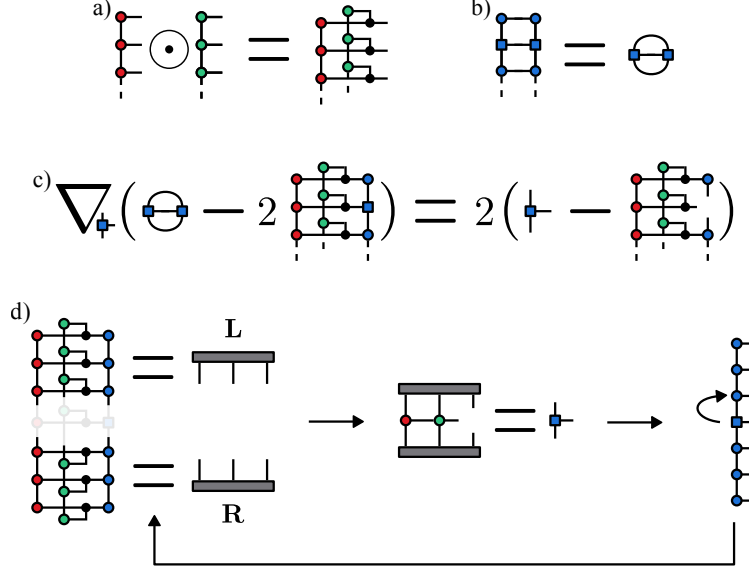


FIG. 9: **Diagrammatic explanation of compressed element-wise multiplication.** The product MPS to be multiplied are depicted with red and green sites, the candidate MPS has blue sites, and small black sites are Kronecker delta tensors. **a)** Diagram for exact element-wise multiplication. Physical dimensions of each MPS site are connected via Kronecker delta tensors (black dots). **b)** Orthogonality conditions simplify inner product of MPS to inner product of canonical centers. **c)** Local gradient with respect to the candidate canonical center of the term to be minimized. **d)** Iteration loop: First the left L and the right side R of the tensor network are contracted. The sites of the product MPS corresponding to the candidate canonical center are contracted with R and L to form the new canonical center. The new center is inserted in the candidate and the canonical center is shifted.

repeat. The contraction of the tensor network scales as $\mathcal{O}(n\chi^4)$ and the shifting of the canonical center can be performed via a QR-decomposition scaling as $\mathcal{O}(\chi^3)$. In all simulations conducted in this work, we take the first product MPS as our candidate $\mathbf{A} = \mathbf{B}$ and iterate through the sites in a sweeping motion $c = 1 \rightarrow c = n \rightarrow c = 1$ two times.

Natural alternatives would be the zip-up algorithm proposed by Stoudenmire et al. [27], which also scales in the bond dimension as $\mathcal{O}(\chi^4)$, or the algorithm proposed by Michaelidis et al. [29] with an improved asymptotic scaling of $\mathcal{O}(\chi^3)$. We chose the iterative method over the alternatives mainly because of our goal to implement MPS-LBM for GPUs using JAX. Using QR-decomposition, the iterative method can be implemented without SVD, which has been shown to be preferable for MPS computations on GPUs [48]. Also both alternative algorithms rely on intermediate results of preferably flexible bond dimensions, which significantly impedes performance gains through JAX [49] just-in-time compilation.

5. Runtime Measurements

In this subsection, we provide data on measured runtimes and discuss them. For all measurements, we performed 100 time steps of the D3Q15 MPS-LBM to compute the mean and standard deviation. In- and outflow conditions, as well as a geometry mask, are enabled. Tensor manipulations were implemented using the Python packages JAX [49] and opt_einsum [50] and all simulations were conducted on an NVIDIA A100 GPU with 80GB of VRAM.

In Figure 10a, the scaling with respect to the number of lattice sites $N = 8^n$ is shown, where n is the

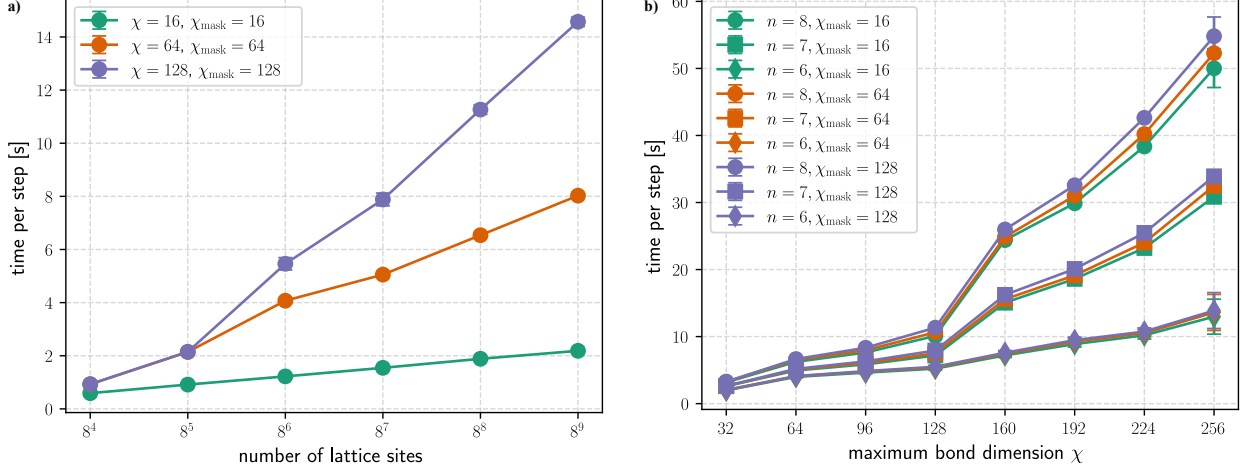


FIG. 10: **Runtime scaling** of a) D3Q15 MPS-LBM with respect to the number of lattice sites b) and the maximum bond dimension.

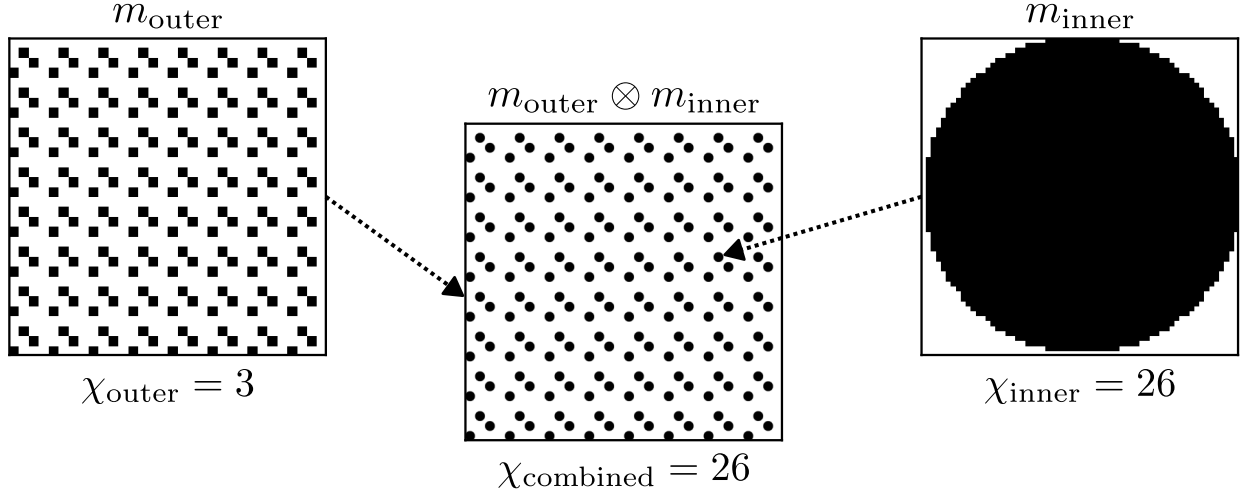


FIG. 11: **Combination of masks on separate length scales.**

number of sites in each MPS for different bond dimension $\chi \in \{16, 64, 128\}$. The expected linear scaling in n is clearly visible. The only deviation at $N = 8^4$ and $N = 8^5$ for $\chi = 128$ is explained by the fact that MPS of these sizes are already exact at a bond dimension of 64, and MPS-LBM hence operates on MPS smaller than the allowed maximum bond dimension of $\chi = 128$.

The scaling with the bond dimension, shown in Figure 10b, is more complex. The scaling with χ^4 cannot clearly be discerned due to an inconsistency between $\chi = 128$ and $\chi = 160$, as well as between $\chi = 224$ and $\chi = 256$. Presumably, these irregularities originate from GPU saturation effects or optimization decisions made by the compiler of JAX [49].

6. Symmetric Geometries in Matrix Product State Decomposition

We examine the relation between MPS decomposition and translationally symmetric geometries using an explicit example, and show that the approach generalizes to realistic cases. Consider a geometry with separation of large- and small-scale structures. We consider an inner geometry represented as a binary mask

m_{inner} of resolution 2^{kD} , repeated according to an outer mask m_{outer} on a 2^{lD} grid. The combined mask inserts the inner geometry at each site where $m_{\text{outer}} = 1$, leaving other sites zero. An example is shown in Figure 11, where the inner mask is a circle on a 64^2 grid, arranged in the repetition pattern defined by an outer mask on a 32^2 grid. For simplicity, in 1D the value at position x is given by

$$m_{\text{combined}}^x = m_{\text{outer}}^{\lfloor x/2^k \rfloor} m_{\text{inner}}^{x \bmod 2^k} = (m_{\text{outer}} \otimes m_{\text{inner}})^x. \quad (\text{A21})$$

Thus, it is straightforward to see that the combined mask is in fact the tensor product of the outer and inner masks. To relate this structure to MPS, we examine the index representation. Consider the scale-ordered decomposition

$$\begin{aligned} \mathbf{x} = x_1 \dots x_D &= b_1^1 \dots b_1^n \dots b_D^1 \dots b_D^n \\ \rightarrow b_1^1 \dots b_D^1 \dots b_1^n \dots b_D^n &= w_1 \dots w_n, \end{aligned} \quad (\text{A22})$$

as used in III C. Let us denote the scale ordered indices of m_{inner} and m_{outer} as $\mathbf{x}_{\text{in}} \rightarrow u_1 \dots u_k$ and $\mathbf{x}_{\text{out}} \rightarrow v_1 \dots v_l$ and consider both masks to be MPS decomposed, then we can write out the tensor product as

$$\begin{aligned} (m_{\text{outer}} \otimes m_{\text{inner}})^{\mathbf{x}_{\text{out}} \mathbf{x}_{\text{in}}} &= m_{\text{outer}}^{v_1 \dots v_l} m_{\text{inner}}^{u_1 \dots u_k} \\ &= \sum_{\{\alpha\}, \{\beta\}} (\mathbf{A}_1)_{\alpha_1}^{v_1} \dots (\mathbf{A}_l)_{\alpha_l}^{v_l} (\mathbf{B}_1)_{\beta_1}^{u_1} \dots (\mathbf{B}_k)_{\beta_k}^{u_k}. \end{aligned} \quad (\text{A23})$$

Therefore, the maximum bond dimension of the combined mask equals the larger of the two masks $\chi_{\text{combined}} = \max(\chi_{\text{outer}}, \chi_{\text{inner}})$. In the example shown in Figure 11, the combined mask has a resolution of 2048^2 and is accurately represented as an MPS with $\chi_{\text{combined}} = 26$. Together with the results from our simulations, this suggests that MPS-LBM would produce physically accurate flows around $\chi \approx 64$ ($\text{CR} \approx 46$). This construction directly relates to the pin-fin scenario, where the inner mask defines a single pin-fin and the outer mask specifies the array layout. The concept generalizes to other applications.